JOURNAL OF MATERIALS SCIENCE 28 (1993) 3205–3213

Microstructure, tensile properties and fracture behaviour of an Al–Cu–Mg alloy 2124

T. S. SRIVATSAN, D. LANNING JR
Department of Mechanical Engineering, The University of Akron, Akron, OH 44325, USA
K. K. SONI
Department of Materials Science and Engineering, Lehigh University, Bethlehem, PA 18015, USA

The microstructure, tensile properties and fracture behaviour of aluminium alloy 2124 were studied. Detailed optical and electron microscopical observations were made to analyse the as-received microstructure of the alloy. It is shown that microstructural characteristics have a profound influence on tensile properties and quasi-static fracture behaviour of the alloy. Tensile test results indicate that the alloy has uniform strength and ductility in the longitudinal and transverse orientations. The elongation and reduction in area are higher in the transverse direction of the extruded plate. No change in fracture mode was observed with direction of testing. Fracture, on a microscopic scale, was ductile, comprising of void nucleation, growth and coalescence. The fracture process is discussed in terms of competing influences of intrinsic microstructural features, deformation characteristics of the matrix and grain-boundary failure.

1. Introduction

The quest for new, improved, high-performance materials to save weight and also provide high durability and damage tolerance in airframe structures, such as, aircraft, space vehicles and lightweight armoured carriers has existed since the advent of powered flight. The stringent demands placed by the newer generation aircraft for high-strength low-density and high-toughness materials resurrected much interest in the development of new aluminium alloys as attractive alternatives to the existing high-strength commercial alloys. In addition, an increase in fuel prices led to an increased pressure for lighter weight structural components primarily because lightweight translates to a decrease in fuel consumption with concomitant savings in operating costs [1–3].

The demand for lighter weight structural components for the aerospace industry led to the development and emergence of aluminium alloy 2024-T3 in 1931 [4]. The alloy contains higher magnesium than aluminium alloy 2017 (1.5% compared with 0.5%) and provided a higher yield strength than 2017-T4, a high ratio of ultimate tensile strength to yield strength, and acceptable strength–ductility relationship. The T3 temper designation recognizes the significant increase in strength attributable to the 1.5%–3.0% stretch applied to rolled and extruded products after quenching to straighten and/or minimize effects of residual quenching stresses. The strength of alloy 2024 was enhanced by imparting cold work prior to artificial ageing treatment (T8 temper). However, the short transverse ductility of alloy 2024-T8 was unacceptable, so efforts to increase this property began in the 1960s. An early solution to this problem was achieved by preforging the ingot prior to rolling to modify the intermetallic particle morphology and distribution that produced stringers during rolling. This solution was found by manufacturers of the material to be uneconomical, so aluminium alloy 2124 was developed. This alloy contained significantly less iron and silicon contents than aluminium alloy 2024, thus reducing the volume fraction of coarse inclusions, and the copper and magnesium contents were controlled to minimize the volume fraction of Mg_2Si and Al_2CuMg constituent particles that could not be dissolved during solution heat treatment.

The objective of this paper is to document the microstructure, tensile properties and fracture characteristics of aluminium alloy 2124. The quasi-static fracture behaviour is examined in the light of competing influences of intrinsic microstructural features and micromechanisms which promote failure.

2. Material and experimental procedure

The 2124 aluminium alloy used in this experimental investigation was provided by DWA Composite Specialties Inc., Chatsworth, CA, as a gift. The alloy was manufactured using well-known powder metallurgy (PM) technique and was provided as an extruded bar of length 350 mm and having a rectangular cross-section, approximately 25 mm thick and 150 mm wide, in the heat-treated condition (modified T4 temper). The heat treatment consisted of solution heat treating the as-extruded alloy at 490 °C for 2 h, followed by cold-water quenching. Subsequent ageing was done at 120 °C for 18 h to give the T4 temper. In order both to speed-up and enhance precipitation, the alloy was artificially aged. The chemical composition (wt%) of the alloy is given in Table I. The alloy is a high-purity version of alloy 2024 with low levels of impurity elements, iron and silicon. Manganese is present in the alloy and plays the role of refining grain size and/or suppressing recrystallization.

Metallographic samples were cut from the three orthogonal directions of the as-received extruded bar. The samples were mounted in bakelite and wet ground on 320, 400 and 600 grit silicon carbide (SiC) paper using water as lubricant and then mechanically polished with 1 μm alumina-based lubricant. The polished specimens were etched using Keller's reagent to reveal the grain boundaries and overall grain morphology. The etched specimens were examined in an optical microscope and micrographs of the longitudinal, long-transverse and short-transverse sections, of the extruded bar, were taken using standard bright-field technique.

Fine microstructural features were revealed by transmission electron microscopy (TEM). Samples 0.5–1.0 mm thick were sliced from the bulk material. Thin foils for TEM investigation were prepared from discs 3 mm diameter, cut, ground and thinned by electropolishing using an electrolyte comprising 30% nitric acid in methanol, at − 20 °C and at a potential difference of 15 V. The foils were examined in a Philips transmission electron microscope at 120 kV.

Blanks of size 20 mm × 20 mm × 150 mm were cut from the as-received plate. Tensile specimens were precision machined from the blanks. The cylindrical test specimens, which conformed to ASTM Standard E-8, with threaded ends and a gauge length which measured 26 mm long and 6.25 mm diameter. The stress axis of the cylindrical samples were parallel (longitudinal) or perpendicular (transverse) to the extrusion direction. To minimize the effects of surface irregularities and finish, final surface preparation was achieved by mechanically polishing the machined surfaces of the test specimens through 600 grit silicon carbide paper to remove all circumferential scratches and machine marks. Uniaxial tensile tests were performed on a computer-controlled closed-loop servo-hydraulic testing machine, equipped with a 10 000 kg load cell, in the room-temperature (23 °C) laboratory-air environment (relative humidity 55%). The specimens were deformed at a constant initial strain rate of $1 \times 10^{-4}\,s^{-1}$. The load and displacements parallel to the load line were recorded on an X–Y recorder. The diameter of the tensile samples was measured using a micrometer, before and after testing.

Fracture surfaces of the deformed tensile specimens were examined in a scanning electron microscope (SEM) in order to determine the predominant fracture mode and to characterize the fine-scale features on the fracture surface.

TABLE I Nominal composition (wt%) of aluminium alloy 2124-T4

Material	Cu	Mg	Mn	Zn	Fe	Si	Al
2124	4.65	1.65	0.9	0.01	0.30	0.04	Bal.

3. Results and discussion

3.1. Initial microstructure

The microstructure of the as-received Al–Cu–Mg alloy is shown in Figs 1 and 2 as triplanar optical micrographs illustrating the grain structure and constituent particle distribution in the three orthogonal directions of the extruded plate. The material is partially recrystallized with the unrecrystallized grains flattened and elongated parallel to the longitudinal direction, as a consequence of deformation introduced during extrusion. At higher magnification, the insoluble and partially soluble constituent particles were observed to be stratified and distributed along the extrusion direction of the plate (Fig. 2). Clustering of constituent particles was seldom observed. The majority of particles were found located along the grain boundaries (Fig. 3a). These second-phase particles are the constituents and are potential nucleation sites for void initiation. The larger constituent particles are the Al_7Cu_2Fe and $Al_{20}Cu_2(FeMn)_3$ [5]. The final size of the coarse constituents depends upon the fabrication procedures and may range in size from 5–30 μm. The smaller particles are the manganese-containing dispersoids ($Al_{20}Cu_2Mn_3$) [6, 7]. They range in size from 0.02–0.5 μm in the longest dimension. The morphology of a constituent particle, located at the grain boundary, is shown in Fig. 3b.

The manganese-containing dispersoids precipitate during the ingot pre-heat and homogenization treatment. These particles play an important role in controlling fracture resistance, because voids formed at the larger constituent particles are linked through void sheet formation at dispersoids. Fig. 4 is a bright-field transmission electron micrograph showing the morphology and distribution of the manganese-containing dispersoids in the aluminium alloy matrix. The silicon content of this alloy is below the solid solubility of silicon in aluminium [8], so no constituent phase containing silicon is present or was observed.

Electron micrographs reveal the fine-scale microstructural details, i.e. dispersoid particles and the morphology and nature of strengthening precipitates. The strengthening precipitates are in the nanometre-size range and form within grain interiors. They control directly the strength and slip behaviour and indirectly influence ductility. The addition of magnesium to binary aluminium–copper alloys enhances both the rate and magnitude of natural ageing. For a fairly high magnesium concentration, the decomposition process or precipitation sequence in an Al–Cu–Mg alloy can be described as

$$\text{Supersaturated solid solution} \rightarrow \text{Guinier–Preston zones} \rightarrow S'' \rightarrow S' \rightarrow S(Al_2CuMg) \qquad (1)$$

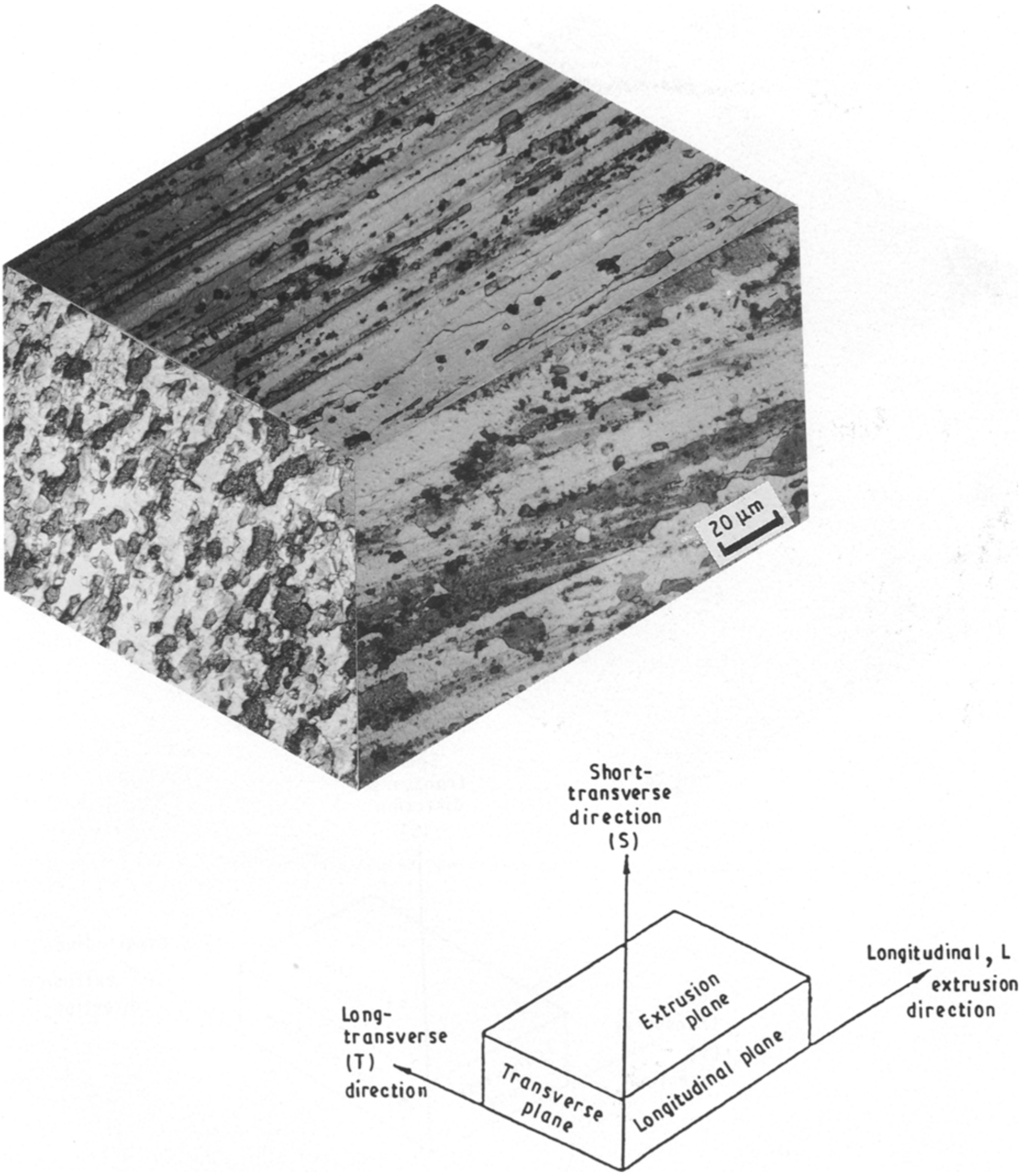

Figure 1 Triplanar optical micrograph illustrating the grain morphology of alloy 2124 extruded plate.

The equilibrium S phase is the intermetallic compound Al_2CuMg [9–11]. The S″ and S′ phases are precursors of the equilibrium S phase, which has been shown to have an orthorhombic crystal structure [11]. The S″ phase is approximately the same as the equilibrium S phase but with a monoclinic lattice and unusual orientation relations with the matrix [11]. The major strengthening phase, in the T4 condition, is predominantly the S′ ($Al_xCu_yMg_z$). The S′ phase is the intermediate or metastable phase of the equilibrium S phase and nucleates on dislocations and grows as laths on {2 1 0} matrix planes along ⟨1 0 0⟩ matrix directions [11]. The orientation relationship of the S′ phase with the matrix is [12]

$$\begin{aligned}
[1\,0\,0]_{\text{matrix}} &\parallel [1\,0\,0]_{S'}\\
[0\,1\,\bar{2}]_{\text{matrix}} &\parallel [0\,0\,1]_{S'}\\
[0\,2\,1]_{\text{matrix}} &\parallel [0\,1\,0]_{S'}
\end{aligned}$$

The transition phase S′ has the same chemical composition and an orthorhombic crystal structure very similar to the equilibrium S phase. Three different morphologies have been proposed for the intermediate S′ phase [12–15]. These are the rod-like phase [11], the lath-like phase [15] and the needle-like phase [13, 14]. Transmission electron microscope observations of the Al–4.65 Cu–1.65 Mg material indicate the S′ phase to be lath-shaped precipitates. The precipitates were located in arrays (Fig. 5). The S′ precipitate is partially coherent with the aluminium matrix [10, 11]. Precipitate-free zones (PFZs) were not found along the grain boundaries or subgrain boundaries of the material (Fig. 6).

3.2. Tensile properties

A compilation of the ambient temperature tensile

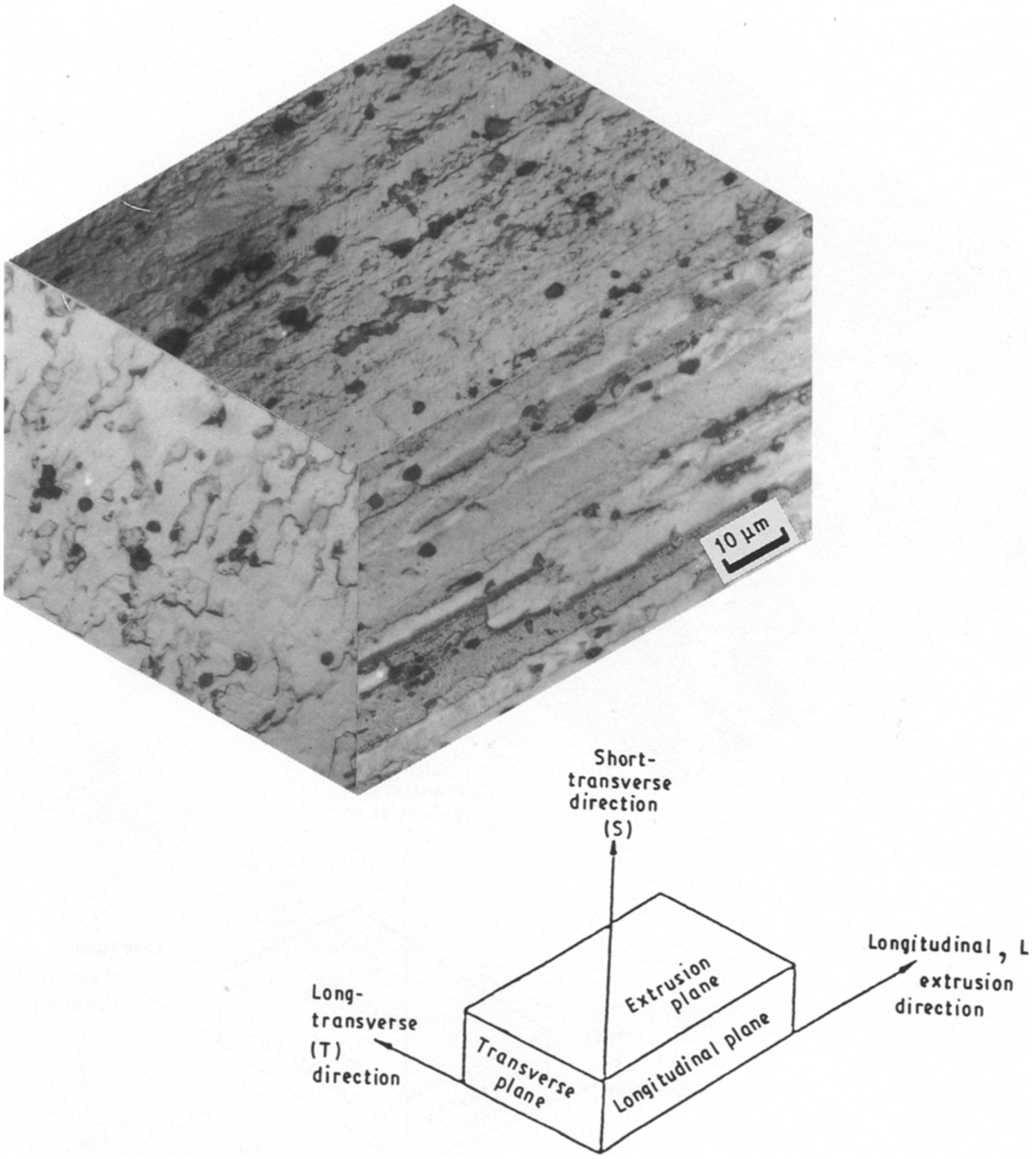

Figure 2 Triplanar optical micrograph illustrating constituent particle density and distribution along the three orthogonal directions of the extruded plate.

properties of aluminium alloy 2124, in the longitudinal (L) and transverse (T) directions, is given in Table II. Duplicate tests were conducted for each condition and no significant variation between the samples was observed.

The yield strength, defined as the stress required at a plastic strain of 0.2%, in the transverse (T) direction (331 MPa) accords well with the corresponding value in the longitudinal direction (327 MPa). The ultimate tensile strength, σ_{UTS} in the transverse direction (481 MPa) also accords well, within limits of allowable experimental error, with the value in the longitudinal direction (491 MPa). The elongation (measured over a 25 mm gauge length) in the transverse direction (22%) shows a 20% improvement over the corresponding value in the longitudinal direction (18%) of the as-received plate. The percentage reduction in area in the transverse direction (32%) also shows an 83% improvement over the corresponding value in the longitudinal direction (17.5%). The true fracture stress in the transverse direction (599 MPa) is 12% higher than the corresponding value in the longitudinal direction (535 MPa), consistent with the higher ductility of the material in the transverse orientation of the as-received plate. The improved ductility and fracture stress in the transverse direction of the extruded plate is attributed, in part, to the distribution of the second-phase particles (constituents and dispersoids). The observed lower volume fraction of constituent particles in the transverse direction than in the longitudinal direction delays microcrack initiation and eventual growth.

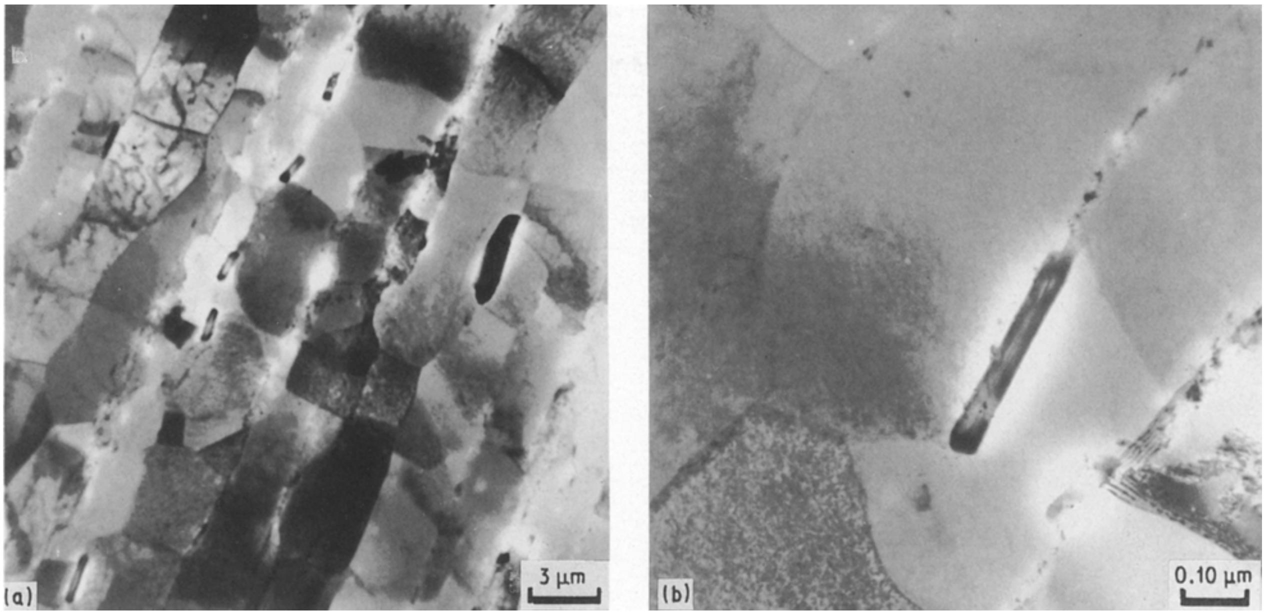

Figure 3 Bright-field transmission electron micrographs showing (a) elongated grains with particles at the grain boundaries, (b) iron-rich constituent particle at the grain boundary.

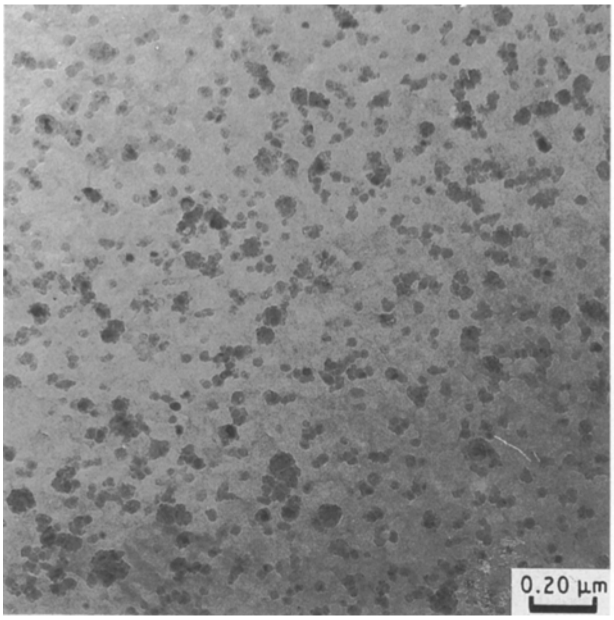

Figure 4 Bright-field transmission electron micrographs showing morphology and distribution of manganese-containing dispersoids.

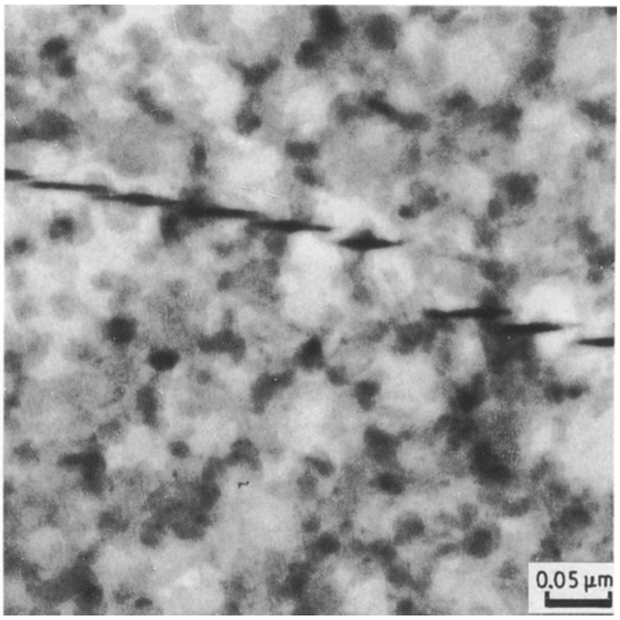

Figure 5 Bright-field transmission electron micrograph showing the morphology of the S′ strengthening precipitate.

The elastic modulus obtained by extensometer trace, accords well in the two directions (longitudinal and transverse). In the T4 temper, the alloy has property combinations which make it an attractive candidate for applications requiring moderate strength and good ductility.

Beyond macroscopic yield the stress–strain curve is well represented by a simple power law. It is expressed by the equation

$$\sigma = k(\varepsilon_p)^n \tag{2}$$

where k is the monotonic strength coefficient (intercept at $\varepsilon_p = 1$) and n is the strain–hardening exponent (the slope). The value of the strain-hardening exponent, determined by least squares fit of Equation 2, is nearly identical in the longitudinal ($n = 0.13$) and transverse ($n = 0.12$) directions. The monotonic stress–strain curve for the alloy is shown in Fig. 7.

3. Fracture behaviour

The monotonic fracture surfaces are helpful in elucidating microstructural effects on the ductility and fracture properties of aluminium alloy 2124. Fractography of the tensile samples revealed fracture to be shear for both the longitudinal and transverse specimens. The fracture surfaces were oriented approximately 40°–50° to the major stress axis, following the plane of maximum shear stress. The shear-type of fracture tends to minimize necking and thus the triaxial state

TABLE II Room-temperature mechanical properties of aluminium alloy 2124-T4

Orientation	Modulus of elasticity[a] (GPa)	0.2% Yield stress (MPa)	UTS (MPa)	Elongation (G.L. = 1 in.)[b] (%)	True strain $\varepsilon_f = \ln(A_o/A_f)$ (%)	Reduction in area (%)	True fracture stress (MPa)
Longitudinal	71	327	491	18	19.2	17.5	535
Transverse	70	331	481	22	38.6	32	599

[a] Tangency measurements based on extensometer trace.
[b] G.L. = gauge length; 1 in. = 2.54 cm.

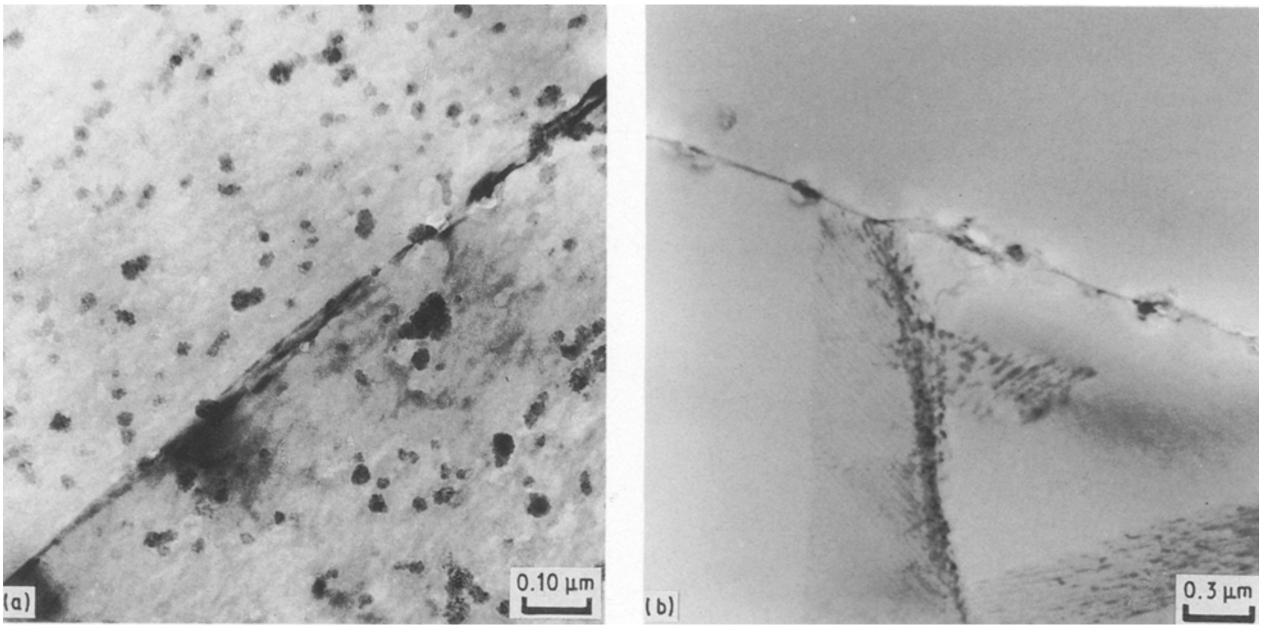

Figure 6 Bright-field transmission electron micrograph showing the absence of precipitate-free zone at the grain boundary.

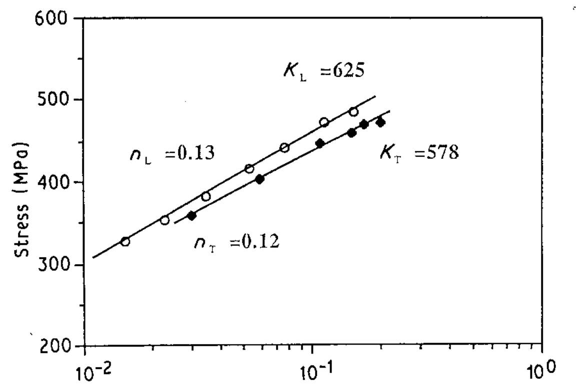

Figure 7 Monotonic stress–strain curve for aluminium alloy 2124: (○) longitudinal, (◆) transverse.

of stress and hydrostatic component that occurs in a necked region [16]. Consequently, void initiation at the coarse constituent particle and subsequent coalescence is affected or influenced. Examination of the fracture surface at high magnification revealed isolated cracking at grain boundaries and features reminiscent of a locally ductile mechanism, that is, void nucleation, growth and coalescence with the nucleation of voids occurring at the coarse constituent particles in the microstructure. Representative fracture features of the samples for both the longitudinal and transverse orientations are shown in Figs 8–10.

On a macroscopic scale, the tensile fracture surfaces of alloy 2124-T4 in the longitudinal and transverse orientations were flat but relatively rough when viewed on a microscale. Long secondary cracks following grain boundaries (Fig. 8a) and a population of microvoids of a wide range of sizes (Figs 8b and 9b) were observed on the fracture surfaces. In the ageing condition studied (T4), it is the nature, size, morphology and distribution of the matrix precipitates that is the important microstructural feature controlling deformation characteristics (slip behaviour) and fracture. The tendency towards localized inhomogeneous deformation due to shearing of the strengthening S′ precipitates dispersed in the matrix results in localization of strain. The planar slip bands resulting from the interaction of dislocations with precipitate particles, impinge upon grain and subgrain boundaries and cause strain concentration or localization at their point of impingement on the grain boundary. The magnitude of strain concentration in the vicinity of grain boundaries depends on the slip length. The

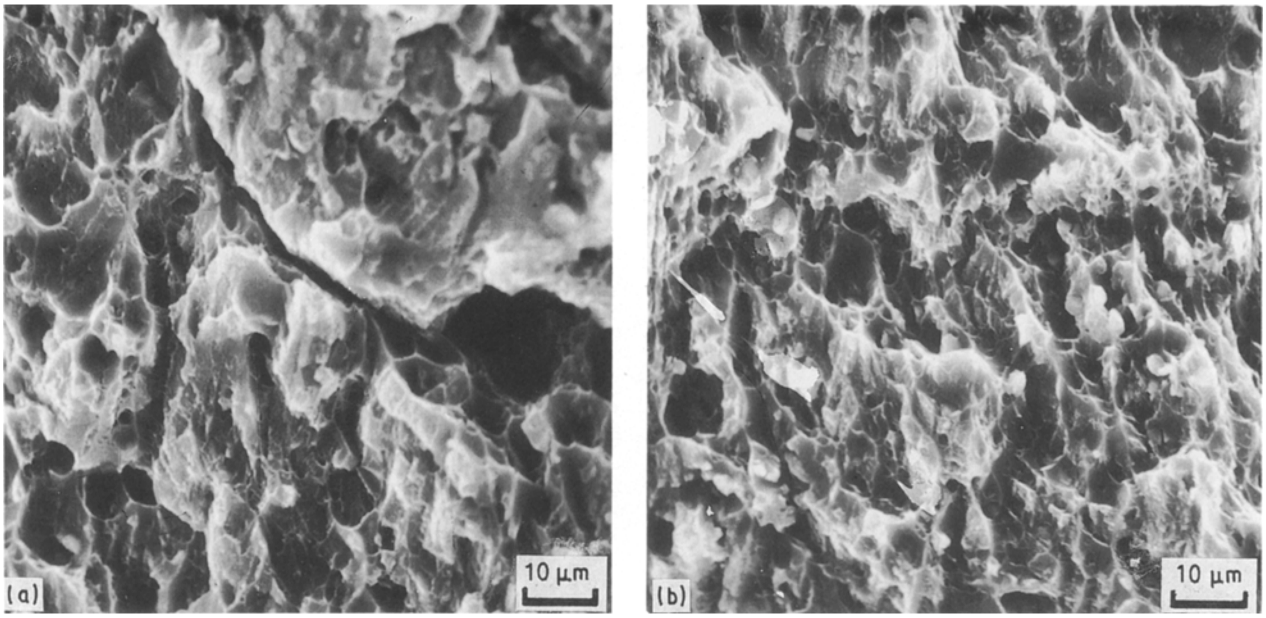

Figure 8 Scanning electron micrographs of fracture surface of longitudinal tensile sample showing (a) cracking along the grain boundary, (b) microvoids of a wide range of sizes.

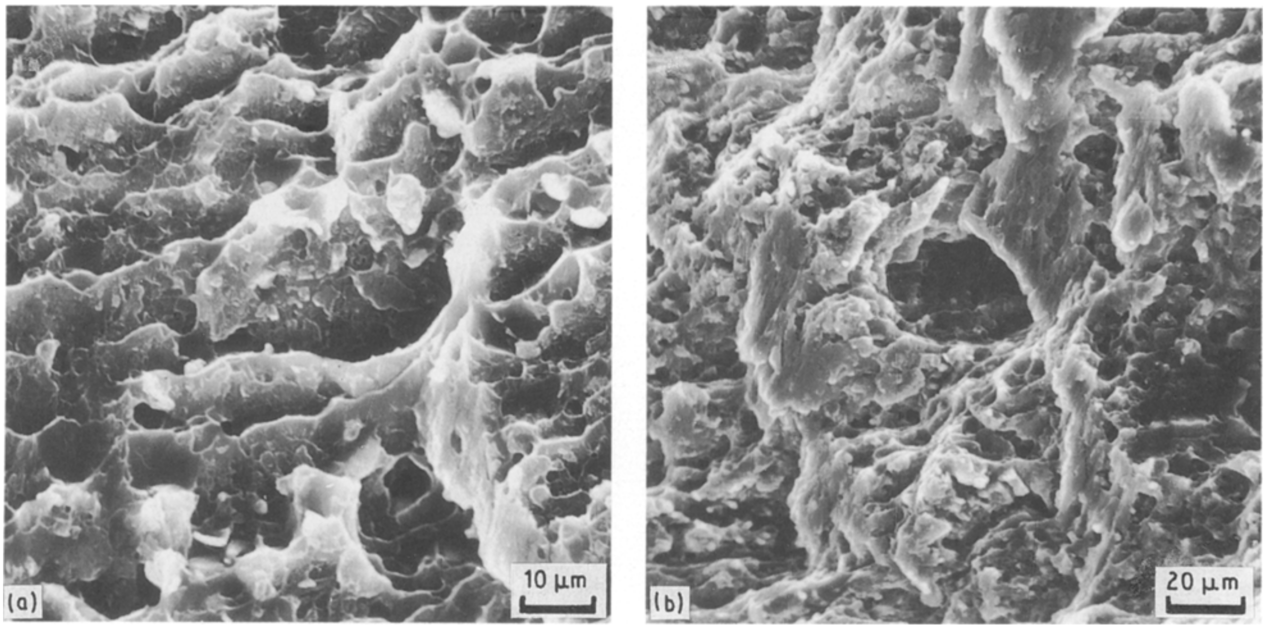

Figure 9 Scanning electron micrographs of the fracture surface of transverse tensile sample showing (a) secondary cracking along subgrain boundaries, (b) macroscopic void on the transgranular fracture surface.

localization of strain and concomitant stress concentration at the termination of the slip band at the grain boundary accelerates the fracture process through the initiation of microcracks at the grain and subgrain boundaries (Figs 8a and 9a), and voids at the coarse constituent particles lying along the grain boundary.

The key microstructural features controlling nucleation of cracks, in this high-purity aluminium alloy, and thus the strain to failure are [17]:

(a) the size, strength, volume fraction and distribution of active second-phase particles or constituents;

(b) the resistance of these constituent particles and their interfaces to decohesion; and

(c) matrix deformation characteristics.

The coarse constituent particles in this high-purity aluminium alloy are predominantly (a) the iron-rich insoluble phases $Al_{20}Cu_2(FeMn)_3$ and Al_7Cu_2Fe [5, 16], and (b) magnesium-rich insoluble phases. No phase containing silicon was present and phase diagrams [8] support this conclusion.

During plastic deformation, nucleation of fine microcracks occurs:

(i) by cracking of the coarse constituent particles [17, 18];

(ii) through decohesion at the particle-matrix interface [18–20]; and

(iii) at areas of poor interparticle bonding [21].

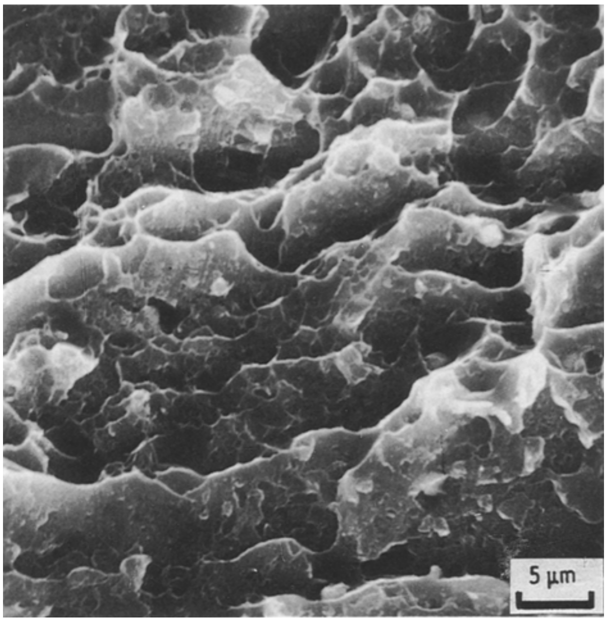

Figure 10 Scanning electron micrographs showing shallow bimodal size dimples on transgranular fracture surface of the longitudinal tensile sample.

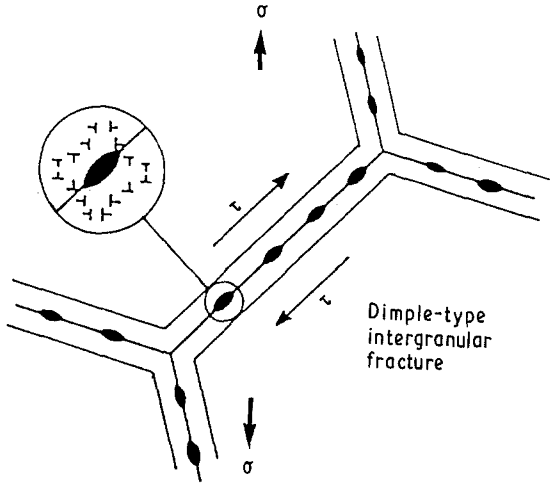

Figure 11 Schematic representation of the dimple-formation type intergranular fracture.

Interfacial strength is a dominant factor in void initiation and microcrack nucleation. Other factors which influence void initiation and growth are [18]: (1) the size of second-phase particles, (2) particle shape and volume fraction, (3) intrinsic strength of the particle, and (4) particle location and distribution. Void initation at the coarse constituent or larger second-phase particles is a complex combination of: (a) inclusion size, (b) stress and local strain levels, and (c) the local deformation mode. The presence of coarse iron-rich constituents, $Al_{20}Cu_2(FeMn)_3$ and Al_7Cu_2Fe, coupled with a matrix microstructure which promotes localized inhomogeneous deformation, facilitates the nucleation of voids at low to moderate stresses. Void nucleation at the coarse constituent particle occurs when the elastic energy in the particle exceeds the surface energy of the newly formed void surfaces [19, 21]. Assuming the coarse second-phase particles to be spherical in shape, the critical stress for particle cracking is

$$\sigma = (6\gamma E/q^2 d)^{1/2} \tag{3}$$

where γ is the surface energy of the particle, q is the local stress concentration factor, E is Young's modulus of the particle, and d is the particle diameter.

While satisfaction of Equation (3) is a necessary condition for void initiation, it must also be aided by a stress on the particle–matrix interface in excess of the interfacial strength [22]. When stress at the particle–matrix interface reaches a critical value, void nucleation occurs by interface separation. In the ageing condition (T4 temper) studied, the interface stress comprises of the applied stress, σ_A, and the normal stress due to blocked slip bands, σ_P

$$\sigma_1 = \sigma_A + \sigma_P \tag{4}$$

When a critical value of σ_1 is reached, void nucleation occurs provided sufficient elastic energy is available to create new void surfaces. Furthermore, in aluminium alloys containing a large volume fraction of second-phase particles or constituent particles there exists an intrinsic particle size and spacing effect on void nucleation [23]. The local stress/strain fields may interact, giving rise to higher levels of local stress/strain than otherwise anticipated, thus enabling void nucleation and growth to be attained at lower applied strains [20]. Progression of this ductile failure mechanism is influenced by the development of plastic strains and stresses during far-field loading. Under the influence of far-field tensile loading, triaxial stresses are generated and the microvoids in the alloy's matrix appear to have undergone limited growth. At certain locations, fine microvoids were observed to be connecting elongated voids. Because crack extension under quasi-static loading occurs at high stress intensities comparable to the fracture toughness of the material, the presence of microvoids tends to degrade the actual strain to failure associated with ductile failure.

Coalescence of the voids and microvoids, formed within the alloy matrix, is a distinctive phase or the last stage in the fracture process. During coalescence void–void interactions occur during which period void growth is accelerated. In this Al–4.65 Cu–1.65 Mg alloy void coalescence results from the formation of void sheets at the smaller second-phase particles, such as the manganese dispersoids ($Al_{20}Cu_2Mn_3$), in conjunction with void impingement, that is, voids growing until they touch. The large voids which are created by fracture of the coarse constituent particles coalesce by impingement. The more widely separated voids coalesce by the formation of void sheets. The halves of the microvoids are the dimples visible on the fracture surface. Coalescence of microvoids initiated at grain-boundary particles results in dimple-formation type of intergranular fracture (Fig. 11). The transgranular fracture regions were covered with a network of very fine shallow dimples (Fig. 10). These dimples are associated with the smaller magnesium-rich insoluble phases and the manganese-containing dispersoids.

4. Conclusions

Based on the results of this investigation on the tensile properties and fracture behaviour of aluminium alloy 2124-T4, the following conclusions are drawn.

1. The alloy is partially recrystallized with the unrecrystallized grains elongated parallel to the extrusion direction.
2. The principal strengthening phase in this alloy is the S′ precipitate with a lath-shaped morphology. There was an absence of precipitate-free zone at grain boundaries and subgrain boundaries.
3. In the T6 condition the yield strength and ultimate tensile strength of the alloy accord well in the longitudinal and transverse directions. The elongation to failure and reduction in area in the transverse direction of the extruded plate showed an improvement over corresponding values in the longitudinal direction. The improvement is attributed to lower volume fraction and fewer agglomeration sites of the coarse constituent particles in the transverse direction.
4. Fracture in both the longitudinal and transverse directions was a combination of cracking along grain and subgrain boundaries with ductile microvoid formation and coalescence.

The results of this study provide useful information on the role of grain structure, coarse second-phase particles, the nature of matrix strengthening precipitates and matrix deformation characteristics on the fracture behaviour of the high-purity Al–4.65 Cu–1.65 Mg–0.9 Mn alloy.

Acknowledgements

This research was partially supported by the Alcoa Foundation (Grant 540341–843, Program Monitor, Dr A.K. Chakrabarti) with material support from DWA Composite Specialties Inc. (Chatsworth, CA, Program Manager, Dr W.C. Harrigan, Jr). K.K.S. thanks the National Science Foundation for support.

References

1. J. T. STALEY *Can. Aeronaut. Space J.* **31** (1) (1985) 14.
2. J. T. STALEY, in "Encyclopedia of Physical Science and Technology", edited by R. Meyers (Academic Press, New York, 1989) p. 177.
3. T. H. SANDERS Jr and J. T. STALEY, in "Fatigue and Microstructure", edited by M. Meshii (ASM, Metals Park, OH, 1979) p. 467.
4. J. T. STALEY, in "Aluminum Alloys: Contemporary Research and Applications", edited by A. K. Vasudevan and R. D. Doherty, Treatise on Materials Science and Technology, Vol. 31, (Academic Press, New York, 1989) p. 5.
5. E. P. BUTLER, N. J. OWEN and D. J. FIELD, *Mater. Sci. Technol.* **1** (1985) 531.
6. E. A. STARKE Jr, in "Aluminum Alloys: Contemporary Research and Applications", edited by A. K. Vasudevan and R. D. Doherty, Treatise on Materials Science and Technology, Vol. 31, (Academic Press, New York, 1989) pp. 48–54.
7. J. A. WALSH, K. V. JATA and E. A. STARKE Jr, *Acta Metall.* **37** (1989) 2861.
8. L. A. WILEY, "Aluminium", Vol. 1, edited by Kent, R. Van Horn (American Society for Metals, Metals Park, OH, 1967) p. 357.
9. JIN YAN, LI CHUNZHI, YAN MINGGAO, *J. Mater. Sci. Lett.* **9** (1990) 421.
10. JIN YAN, *ibid.* **10** (1991) 591.
11. A. K. GUPTA, P. GAUNT, M. C. CHATURVEDI, *Phil. Mag. A* **55** (1987) 375.
12. J. M. SILCOCK, *J. Inst. Metals* **89** (1961) 203.
13. S. HISASHI and K. MOTOHIRO, *J. Jpn Inst. Light Metals* **31** (1981) 277.
14. R. E. SANDERS Jr, T. H. SANDERS, Jr, and J. T. STALEY, *Aluminium* **59** (1983) p. 143.
15. R. N. WILSON and P. G. PARTRIDGE, *Acta Metall.* **13** (1965) 321.
16. W. X. FENG, F. S. LIN and E. A. STARKE Jr, *Metall. Trans.* **15A** (1984) 1209.
17. R. H. VAN STONE, R. H. MERCHANT and J. R. LOW Jr, in "Fatigue and Fracture Toughness, Cryogenic Behavior", ASTM STP 556, (American Society for Testing and Materials, Philadelphia, PA, 1974) p. 124.
18. A. W. THOMPSON, *Metall. Trans.* **18A** (1987) 1877.
19. J. GURLAND and J. PLATEAU, *Trans. ASM* **56** (1963) 442.
20. R. H. VAN STONE and J. A. PSIODA, *Metall. Trans.* **6A** (1975) 672.
21. R. H. VAN STONE, T. B. COX, J. R. LOW Jr and J. A. PSIODA, *Int. Met. Rev.* **30** (1985) 157.
22. A. S. ARGON, J. IM and R. SAFOGLU, *Metall. Trans.* **6A** (1975) 825.
23. A. S. ARGON, *J. Engng Mater. Technol.* **98** (1976) 60.

Received 16 January
and accepted 20 November 1992